LEGIBILITY NOTICE

14/ 8/13/87 JS (2)

(5)

DR-0288-7

I-31519

ORNL/FEDC-87/3

ELASTIC-PLASTIC ANALYSIS OF THE TOROIDAL FIELD COIL INNER LEG OF THE COMPACT IGNITION TOKAMAK

T. Horie

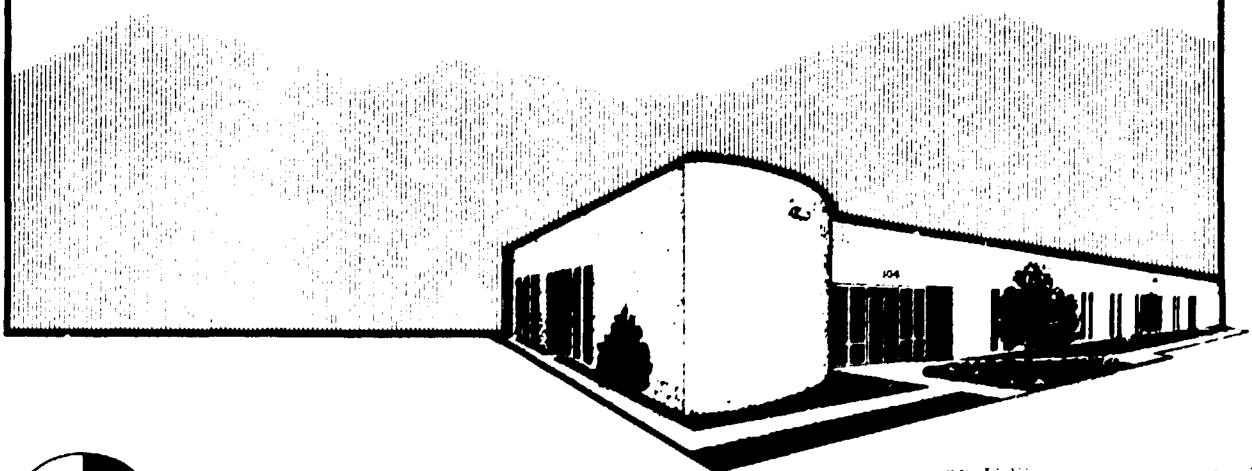

DISTRIBUTION OF THIS ...

FUSION ENGINEERING DESIGN CENTER

OAK RIDGE NATIONAL LABORATORY Operated by MARTIN MARIETTA ENERGY SYSTEMS, INC.

Printed in the United States of America. Available from
National Technical Information Service
U.S. Department of Commerce
5285 Port Royal Road, Springfield, Virginia 22161
NTIS price codes--Printed Copy: A03; Microfiche A01

ORNL/FEDC-87/3
Dist. Category UC-20c, d

ORNL/FEDC--87/3

DE87 013377

Fusion Energy Division

ELASTIC-PLASTIC ANALYSIS OF THE TOROIDAL FIELD COIL INNER LEG OF THE COMPACT IGNITION TOKAMAK

T. Horie

Fusion Engineering Design Center, Oak Ridge National Laboratory
and
Department of Large Tokamak Research, Japan Atomic Energy Research Institute

Date Published: July 1987

Prepared by the
OAK RIDGE NATIONAL LABORATORY
Oak Ridge, Tennessee 37831
operated by
MARTIN MARIETTA ENERGY SYSTEMS, INC.
for the
U.S. DEPARTMENT OF ENERGY
under contract DE-AC05-84OR21400

MASTER

CONTENTS

ABSTRACT

Elastic-plastic analyses were made for the inner leg of the Compact Ignition Tokamak toroidal field (TF) coil, which is made of copper-Inconel composite material. From the result of the elastic-plastic analysis, the effective Young's moduli of the inner leg were determined by the analytical equations. These Young's moduli are useful for the three-dimensional, elastic, overall TF coil analysis.

Comparison among the results of the baseline design ($R = 1.324$ m), the bucked pressless design, the 1.527-m major radius design, and the 1.6-m major radius design was also made, based on the elastic-plastic TF coil inner leg analyses.

1. INTRODUCTION

Copper-Inconel composite material is being considered for use for the inner leg of the Compact Ignition Tokamak[1] (CIT) toroidal field (TF) coils. Since the copper of the composite deforms plastically by the face compression loading to support the centering force, elastic-plastic finite element analysis is inevitable for the coil design. The purpose of the analysis was to determine the effective Young's moduli of the composite and to examine more closely the inner leg behavior for various CIT alternative designs.

An analytical relation is used here to determine the effective Young's modulus from the results of the elastic-plastic finite element analysis. The effective Young's moduli are useful for three-dimensional overall coil analysis to reduce computer time. Elastic analysis with the effective Young's moduli was also made to check the accuracy of this method.

Elastic-plastic analyses of various CIT alternative designs were also made for the baseline design, the shear force model, the bucked pressless design, various press models, the 1.527-m major radius design, and the 1.6-m major radius design for comparison and selection of the design.

2. METHOD OF ANALYSIS

2.1 EFFECTIVE YOUNG'S MODULI OF THE COMPOSITE BASED ON ELASTIC-PLASTIC FINITE ELEMENT ANALYSIS

Stress-strain relations in a three-dimensional elastic body are written as

$$\epsilon_x = \frac{\sigma_x}{E_x} - \frac{\nu_{yx}}{E_y}\sigma_y - \frac{\nu_{zx}}{E_z}\sigma_z \ , \tag{1}$$

$$\epsilon_y = -\frac{\nu_{xy}}{E_x}\sigma_x + \frac{\sigma_y}{E_y} - \frac{\nu_{zy}}{E_z}\sigma_z \ , \tag{2}$$

$$\epsilon_z = -\frac{\nu_{xz}}{E_x}\sigma_x - \frac{\nu_{yz}}{E_y}\sigma_y + \frac{\sigma_z}{E_z} \ , \tag{3}$$

where ϵ, σ, ν, and E are strain, stress, Poisson ratio, and Young's modulus, respectively. From the Betti reciprocal theory of

$$\frac{\nu_{yx}}{E_y} = \frac{\nu_{xy}}{E_x} \ , \tag{4}$$

$$\frac{\nu_{zx}}{E_z} = \frac{\nu_{xz}}{E_x} \ , \tag{5}$$

$$\frac{\nu_{zy}}{E_z} = \frac{\nu_{yz}}{E_y} \ , \tag{6}$$

and the assumption that

$$\nu_{yx} = \nu_{zx} = \nu_{zy} = 0.3 \ , \tag{7}$$

Eqs. (1)–(3) are rewritten as

$$\epsilon_x = \frac{\sigma_x}{E_x} - \frac{0.3}{E_y}\sigma_y - \frac{0.3}{E_z}\sigma_z \ , \tag{8}$$

$$\epsilon_y = -\frac{0.3}{E_y}\sigma_x + \frac{\sigma_y}{E_y} - \frac{0.3}{E_z}\sigma_z \ , \tag{9}$$

$$\epsilon_z = -\frac{0.3}{E_z}\sigma_x - \frac{0.3}{E_z}\sigma_y + \frac{\sigma_z}{E_z} \ . \tag{10}$$

From Eqs. (8)–(10), the Young's moduli are expressed as

$$E_z = \frac{1}{\epsilon_z}(\sigma_z - 0.3\sigma_x - 0.3\sigma_y) \ , \tag{11}$$

$$E_y = \frac{\sigma_y - 0.3\sigma_x}{\epsilon_y + (0.3/E_z)} \ , \tag{12}$$

$$E_x = \frac{\sigma_x}{\epsilon_x + (0.3/E_y)\,\sigma_y + (0.3/E_z)\,\sigma_z} \quad . \tag{13}$$

If averaged stress and strain components obtained from the elastic-plastic finite element method are used in Eqs. (11)–(13), E_x, E_y, and E_z will be the effective Young's moduli, including the effect of plastic deformation.

2.2 METHOD OF FINITE ELEMENT ANALYSIS

The general-purpose finite element code MSC/NASTRAN[2] was used in the analyses. Three-dimensional eight-node isoparametric elements, isotropic material properties, von Mises yield criterion, associated flow rule, and BFGS quasi Newton-Raphson method for each load increment were used here.

2.3 MODEL OF THE ANALYSIS

A model of a half turn of the inner leg with an arbitrary vertical length is shown in Fig. 1. Boundary conditions, which simulate the face compression actual loading condition, are also shown. Figures 2 and 3 show the mesh subdivision and the size of the model, respectively. The model is based on the baseline ($R = 1.324$-m) design.

In the analysis, the copper was regarded as an elastic-plastic material whose stress-strain curve[3] is approximated by linear interpolation from five points, whereas both the Inconel and the insulator were regarded as elastic materials. Material properties used are summarized in Table 1.

2.4 APPLIED FORCE OF THE ANALYSIS

According to the electromagnetic force and the reaction force calculation,[4,5] the electromagnetic centering force in the copper is 1.12 GN/m^3, and the preload required for canceling the electromagnetic tensile force is 436 kN/half turn for the baseline machine ($R = 1.324$ m, revised shape). The forces were applied in the sequence corresponding to actual CIT machine operation. The vertical compression load was applied first; the vertical force was then decreased to zero as the magnetic centering force was increased (Fig. 4).

ORNL–DWG 87-2303 FED

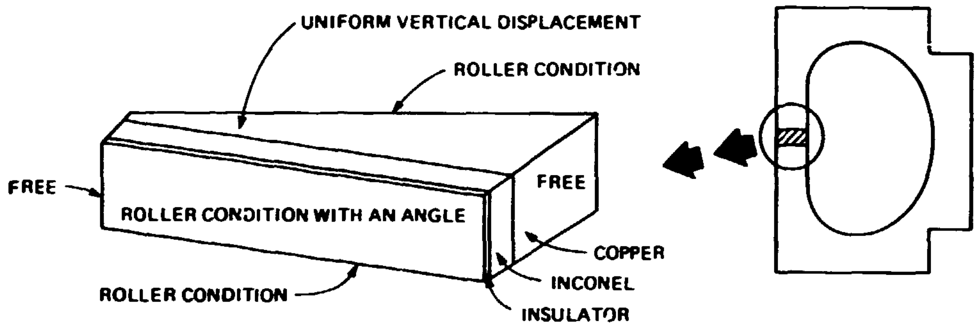

Fig. 1. Model and boundary conditions of the half turn of the inner leg.

ORNL–DWG 87-2304 FED

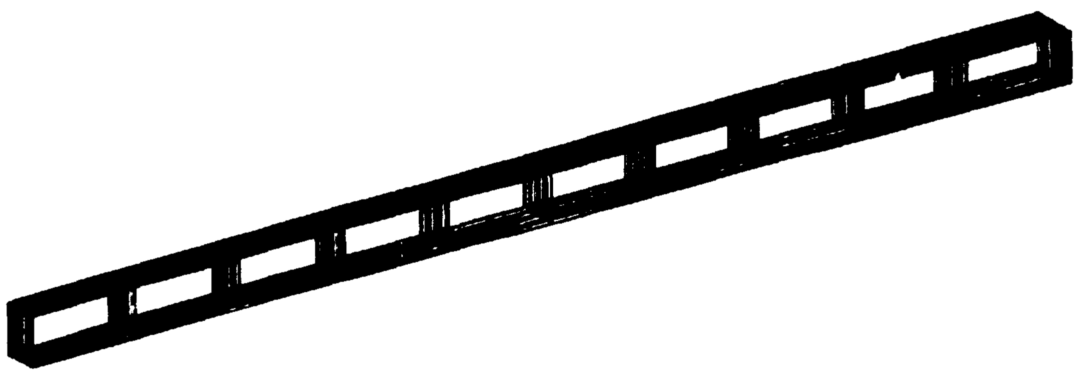

Fig. 2. Mesh subdivision of the inner leg of the TF coil with 120 eight-node isoparametric elements.

ORNL–DWG 87-2305 FED

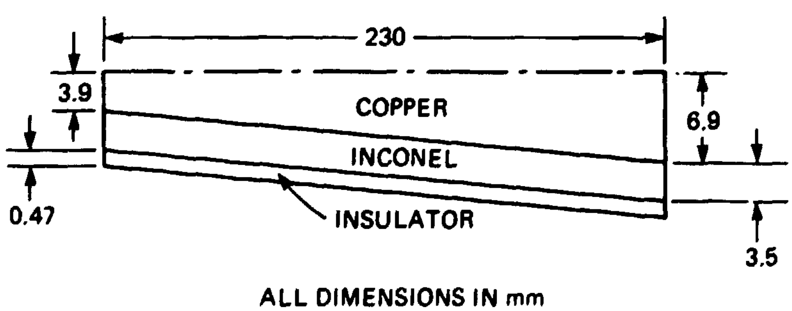

COPPER: 57.5% 16 COILS
INCONEL: 37.5% 15 TURNS/COIL
INSULATOR: 5.0%

Fig. 3. Size of the model of the inner leg for the baseline (R = 1.324-m) design.

Table 1. Material properties used in analysis

Stress-strain relation of copper

Strain (%)	Stress (MPa)
0	0
0.24	258
0.36	303
0.58	310
1	312

Young's modulus and Poisson ratio

	Young's modulus (GPa)	Poisson ratio
Copper	107	0.3
Inconel	207	0.3
Insulator	10.3	0.3

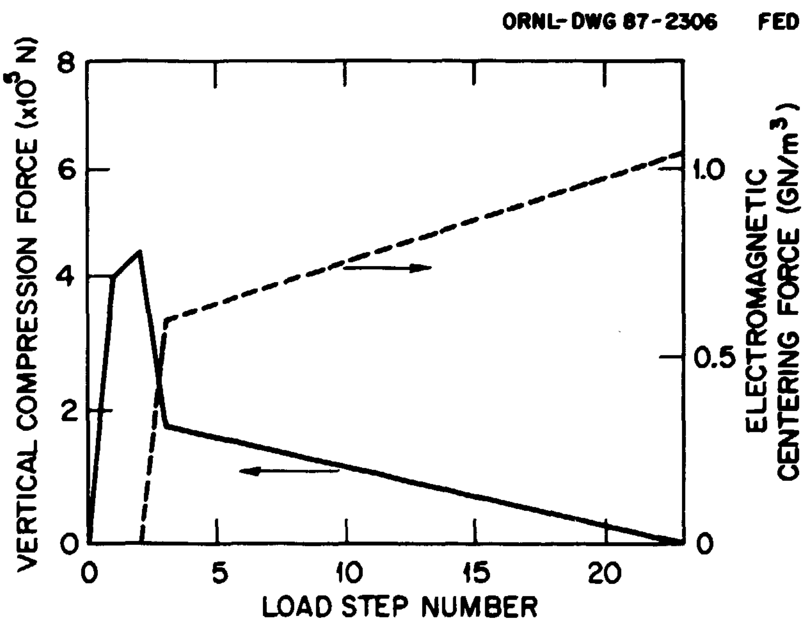

Fig. 4. Loading history of vertical and centering force in the analysis.

3. RESULTS OF THE EFFECTIVE YOUNG'S MODULUS OF THE CIT TF COIL

3.1 EFFECTIVE YOUNG'S MODULUS BY ELASTIC-PLASTIC FINITE ELEMENT ANALYSIS

The effective Young's modulus obtained by the elastic-plastic finite element analysis is compared with the moduli obtained by the elastic mixture rule and elastic finite element analysis.

The elastic mixture rule of Young's modulus for three layers is extended from that of two layers,[6] such as

$$\frac{1}{E_f} = \frac{\alpha_{Cu}}{E_{Cu}} + \frac{\alpha_{Inc}}{E_{Inc}} + \frac{\alpha_I}{E_I} + \frac{2\nu^2}{1-\nu^2}\left(\frac{1}{E_{Cu}} - \frac{1}{E_{Inc}}\right)$$

$$\times \left([\alpha_{Cu}\alpha_{Inc}E_I(E_{Cu} - E_{Inc})^2 + \alpha_{Inc}\alpha_I E_{Cu}(E_{Cu} - E_{Inc})(E_I - E_{Inc})\right.$$

$$+ \alpha_I\alpha_{Cu}E_{Inc}(E_{Cu} - E_I)^2]$$

$$\times \{E_I[E_{Cu}(E_{Cu} - E_{Inc})\alpha_{Cu} + E_{Inc}(E_{Cu} - E_{Inc})\alpha_{Inc}$$

$$\left. + (E_{Cu}^2 - E_{Inc}E_I)\alpha_I]\}^{-1}\right) \tag{14}$$

for face compression direction and

$$E_i = \alpha_{Cu}E_{Cu} + \alpha_{Inc}E_{Inc} + \alpha_I E_I \tag{15}$$

for in-plane direction, where α is the thickness fraction of the composite and subscripts Cu, Inc, and I are copper, Inconel, and insulator.

Effective Young's moduli obtained are summarized in Table 2. There are slight differences between the values obtained by the elastic mixture rule and the elastic finite element analysis; these seem to be caused by the infinite length and wedge-shape geometry of the inner leg of the TF coil. According to the result of elastic-plastic finite element analysis, the effective Young's moduli are decreased about 20 to 40% by the plastic deformation of the copper. Figure 5 shows the decrease of

Table 2. Effective Young's moduli

	E_f (GPa)	E_r (GPa)	E_v (GPa)
Elastic mixture rule	88.6	140.2	140.2
Elactic finite element analysis	93.0	140.8	136.7
Elastic-plastic finite element analysis	73.7	84.9	94.3

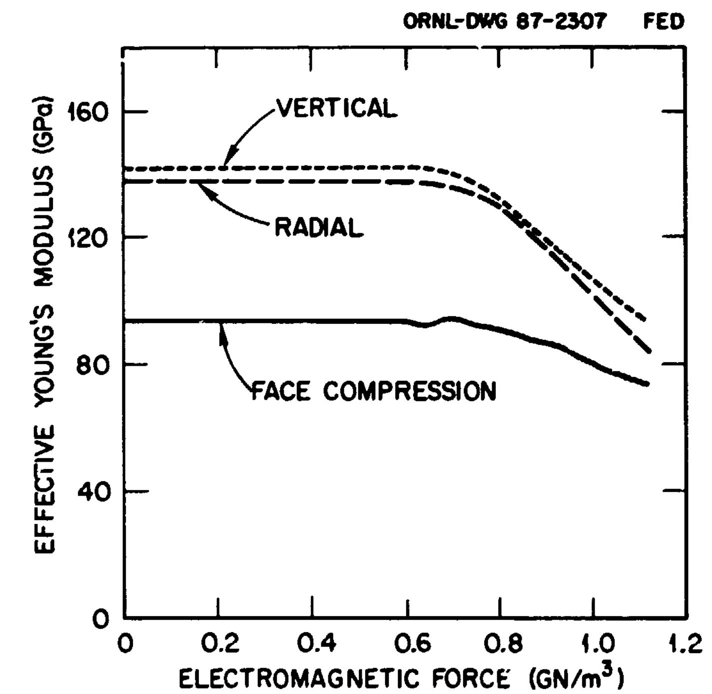

Fig. 5. Decrease of effective Young's modulus during electromagnetic loading.

the effective Young's moduli during the loading of the electromagnetic centering force. Since the effective Young's moduli are different for different loading values, a similar analysis is needed for each design.

3.2 COMPARISON BETWEEN ELASTIC-PLASTIC ANALYSIS AND ELASTIC ANALYSIS WITH EFFECTIVE YOUNG'S MODULUS

To examine the validity of the effective Young's modulus, elastic analysis with the use of the effective Young's moduli obtained by elastic-plastic analysis was performed and compared with the results of the elastic-plastic finite element analysis. In the elastic analysis, mesh subdivision and boundary conditions were the same as for the elastic-plastic analysis, whereas all elements had anisotropic effective Young's moduli. Average stress and strain are compared in Table 3. Since agreement between the two analyses is very good, the elastic analysis with the use of the effective Young's moduli is useful especially for the overall TF coil analysis from the viewpoint of computer time.

4. ELASTIC-PLASTIC ANALYSES OF VARIOUS CIT DESIGNS

Elastic-plastic finite element analyses of the TF coil inner legs of various alternative designs were made to compare plastic deformation in the designs.

4.1 BASELINE (ORIGINAL SHAPE) MODEL

Analysis conditions of the baseline (original) model are summarized in Table 4. The mesh subdivision, boundary conditions, and material properties were the same as those given in Sect. 2.

Figure 6 shows the displacement of the TF coil toward the center. The TF coils move 0.33 mm outward when preload is applied and then move 4.1 mm inward when electromagnetic force is applied. Figures 7 through 9 show the stress distributions through the composite for the inner side, the center, and the outer side of the inner leg, respectively. The stress level is higher on the inner side, and the stress distribution has a peak at the interface of the copper and the Inconel, especially

Table 3. Comparison of stress and strain from the elastic-plastic analysis and the elastic analysis with effective Young's moduli

Stress and strain[a]	Elastic-plastic analysis	Elastic analysis with effective Young's moduli
Stress, MPa		
σ_f	−462.7	−463.4
σ_r	−11.0	−12.2
σ_v	−0.06	−0.02
Strain, %		
ϵ_f	−0.623	−0.619
ϵ_r	−0.151	−0.150
ϵ_v	−0.151	−0.150

[a]Subscripts *f*, *r*, and *v* indicate face compression direction, radial direction, and vertical direction, respectively.

ORNL–DWG 87-2314 FED

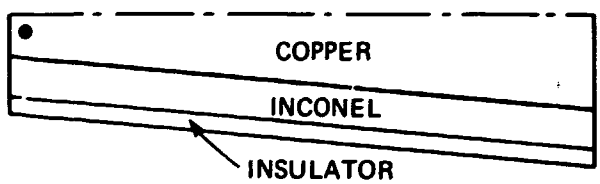

Table 4. Analysis conditions of the baseline (original) model

Thickness, mm	
Copper	6.9/3.9
Inconel	3.5
Insulator	0.47
Width of inner leg, mm	230
Electromagnetic force	
Centering, GN/m^3	1.03
Hoop, kN/half turn	556
Preload, kN/half turn	−556
Number of coils	16
Number of turns per coil	15

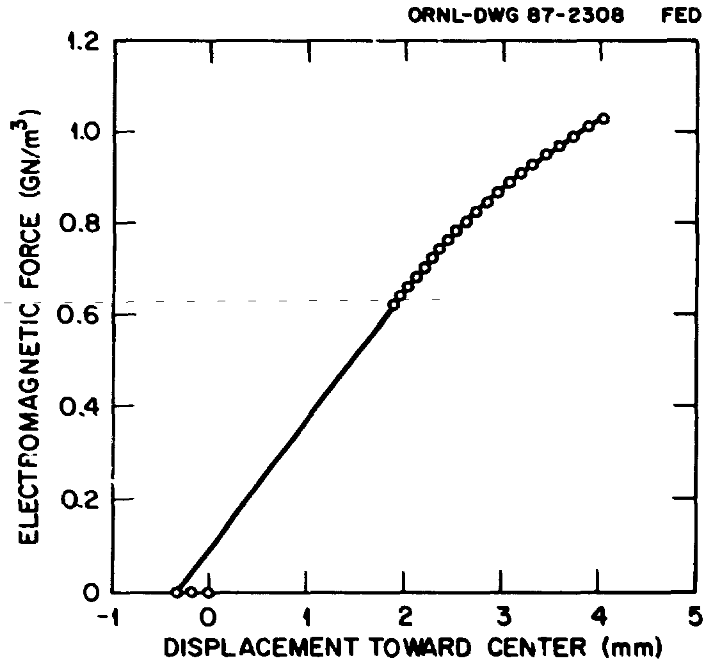

Fig. 6. Displacement of TF coil inner leg.

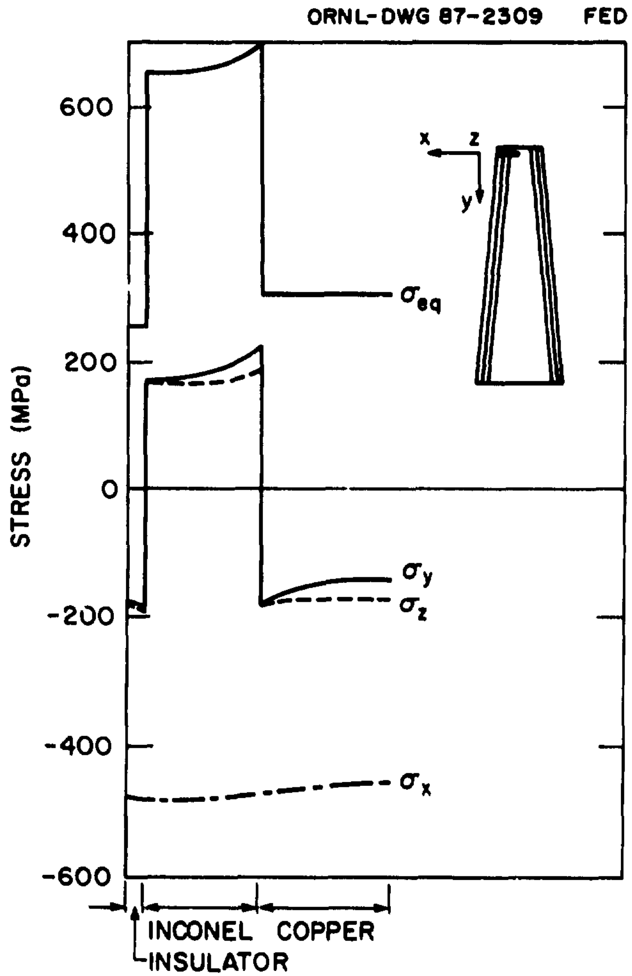

Fig. 7. Stress distribution along the inner surface for the baseline (original) design.

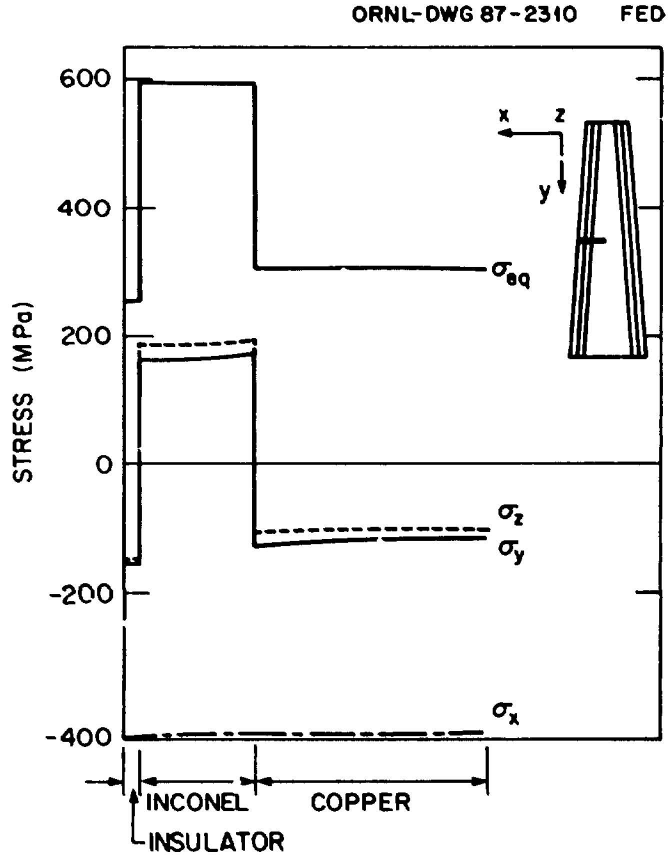

Fig. 8. Stress distribution along the center for the baseline (original) design.

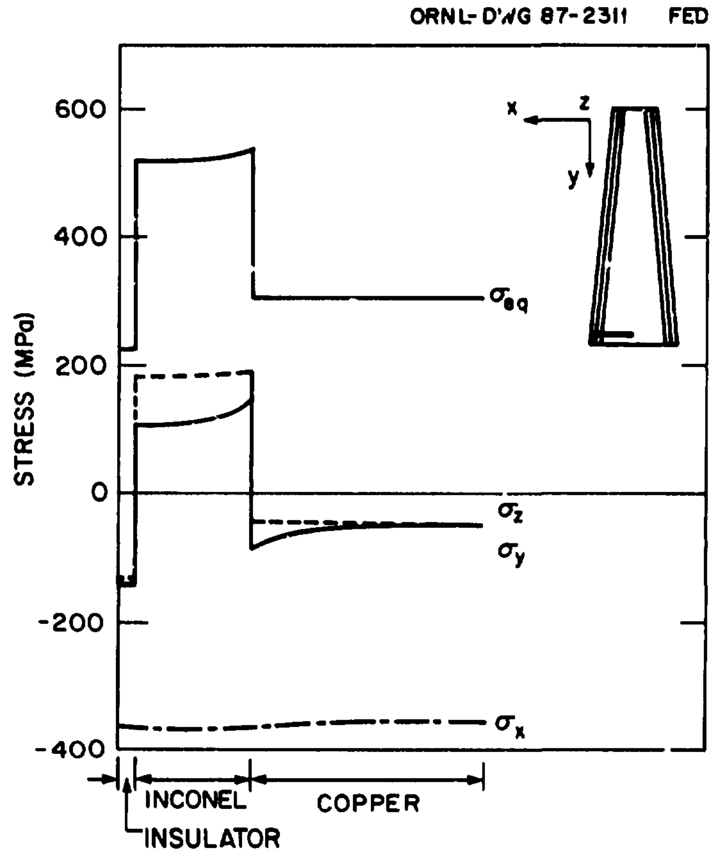

Fig. 9. Stress distribution along the outer su ace for the baseline (original) design.

near the side by the edge effect. Equivalent stress in the copper is almost uniform since the copper is in the flat part of the stress-strain curve.

4.2 BASELINE WITH SHEAR MODEL

The baseline design was analyzed with shear force, which results from the out-of-plane load of TF coils, to examine the effect of the shear force. Shear traction force of 13.8 MPa (2 ksi) for normal operation and 20.7 MPa (3 ksi) extra for disruption was applied on the side surface of the TF coil. Other conditions were the same as those for the previous analysis for the baseline model.

Figure 10 shows the stress and strain distribution along the inner surface of the TF coil for normal operation, and Tables 5 and 6 give the stress and strain in the copper and the Inconel, respectively. The 13.8-MPa shear traction force produces only a slight increase (3%) in the maximum equivalent plastic strain in the copper compared with the plastic strain for the baseline forces. However, it increases significantly (13%) for the disruption forces.

4.3 BUCKED PRESSLESS MODEL

In the bucked pressless model, displacement in the radial direction was constrained by bucking on the inner surface of the coil. Since no preload was applied, tensile stress occurred in the vertical direction. Other conditions were the same as those for the previous analysis. Stress distribution through the composite is shown in Fig. 11, and the stress and strain on the inner side for the copper and the Inconel are given in Tables 7 and 8, respectively. Since the centering force was mostly supported by the Inconel in the bucked design, no face compression stress occurred, and the maximum equivalent stress in the copper was reduced to 258 MPa, which is below the yield stress, from 310 MPa for the baseline design.

4.4 REVISED BASELINE AND VARIOUS PRESS MODELS

Analyses were made for half-press and no-press cases to examine the effectiveness of the press system that reduces the stress in the copper. Analysis for the

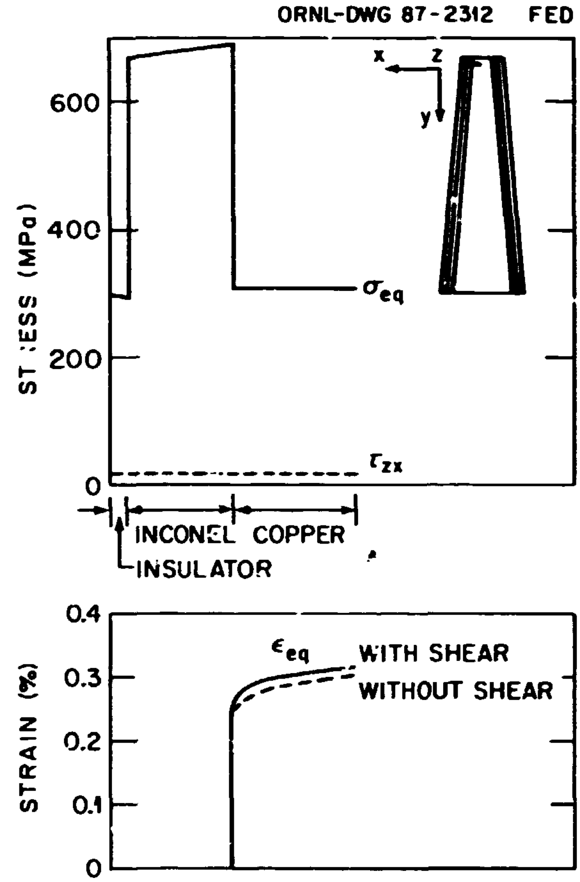

Fig. 10. Stress and strain distribution for normal operation for the shear model.

49% loading operation with and without press was also made to determine if the press system is needed for half-loading operation. According to the CIT design specification, the machine will be operated for 50,000 cycles in a 70% magnetic field (49% electromagnetic force) and for 3000 cycles in a 100% field. These analyses were based on a revised baseline (R = 1.324-m) machine which has the same shape and size of the original baseline (R = 1324-m) machine but which uses a different electromagnetic force. Analysis conditions are summarized in Table 9.

Tables 10 and 11 compare stress and strain in the copper and the Inconel, respectively. For the 100% loading case, the equivalent plastic strain in the copper for the no-press case was 1.5 times as large as that of the press case. These values should be checked by fatigue test to confirm the effectiveness of the press system.

Table 5. Stress and strain within copper at the inner surface for baseline and baseline with shear models

Stress and strain[a]	Baseline (MPa)	Baseline with shear (MPa)	
		2 ksi	5 ksi
σ_f	−463	−463	−464
σ_r	−138	−140	−148
σ_v	−170	−170	−171
τ_{fr}	3.8	3.9	4.1
τ_{rv}	0	0	0.01
τ_{vf}	0	13.5	34.2
σ_{eq}	310	310	310
$\epsilon_{eq}^{(p)}$	0.31%	0.32%	0.35%

[a]Subscripts f, r, and v indicate face compression direction, radial direction, and vertical direction, respectively.

ORNL–DWG 87-2314 FED

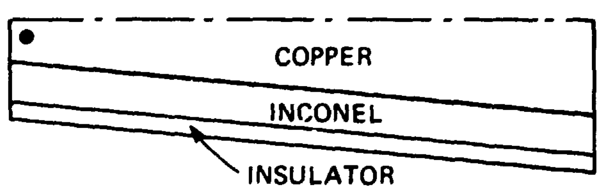

Table 6. Stress and strain within Inconel at the inner surface for baseline and baseline with shear models

Stress and strain[a]	Baseline (MPa)	Baseline with shear (MPa)	
		2 ksi	5 ksi
σ_f	−478	−479	−480
σ_r	210	216	227
σ_v	181	200	230
τ_{fr}	41.3	42.8	45.4
τ_{rv}	0	−0.17	0.25
τ_{vf}	0	13.7	34.4
σ_{eq}	678	691	715
$\epsilon_{eq}^{(p)}$	0%	0%	0%

[a]Subscripts f, r, and v indicate face compression direction, radial direction, and vertical direction, respectively.

ORNL–DWG 87-2314A FED

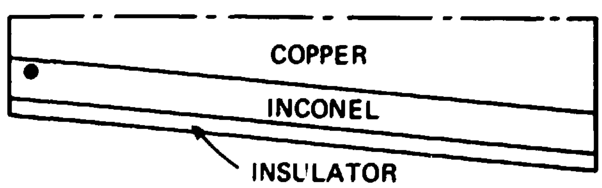

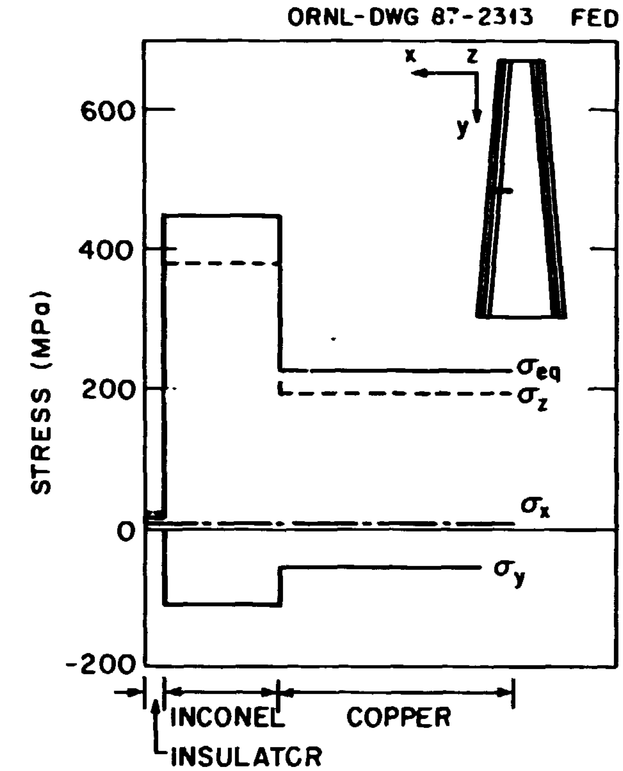

Fig. 11. Stress distribution for the bucked pressless design.

Equivalent stress in Inconel for the no-press case was also 1.5 times as large as that of the press case. However, this value of 1113 MPa is very close to the yield stress of the Inconel. The result of the half-press case is approximately midway between the press and the no-press case.

For the 49% loading case, stress and strain in both the copper and the Inconel for the no-press case were so small that preload was not needed for the baseline (R = 1.324-m) machine in the 70% field operation.

4.5 ALTERNATIVE LARGER MACHINE MODEL

Analyses of alternative designs with 1.527- and 1.6-m major radii without a press system were made and compared with the baseline machine. Analysis for different fractions of copper and Inconel was also made for the 1.6-m machine to

Table 7. Comparison of stress and strain within copper at the inner surface for baseline and bucked pressless models

Stress and strain[a]	Baseline (MPa)	Bucked pressless (MPa)
σ_f	−463	12.7
σ_r	−138	−116
σ_v	−170	180
τ_{fr}	3.8	0.26
τ_{rv}	0	0
τ_{vf}	0	0
σ_{eq}	310	258
$\epsilon_{eq}^{(p)}$	0.31%	0%

[a]Subscripts f, r, and v indicate face compression direction, radial direction, and vertical direction, respectively.

ORNL–DWG 87-2314 FED

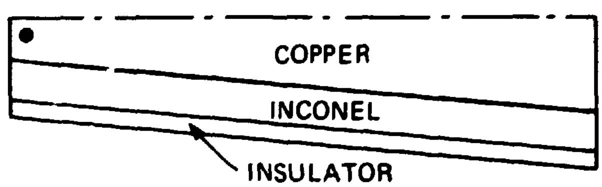

Table 8. Comparison of stress and strain within Inconel at the inner surface for baseline and bucked pressless models

Stress and strain[a]	Baseline (MPa)	Bucked pressless (MPa)
σ_f	−478	12.1
σ_r	210	−229
σ_v	181	343
τ_{fr}	41.3	2.97
τ_{rv}	0	0
τ_{vf}	0	0
σ_{eq}	678	498
$\epsilon_{eq}^{(p)}$	0%	0%

[a]Subscripts f, r, and v indicate face compression direction, radial direction, and vertical direction, respectively.

ORNL–DWG 87-2314A FED

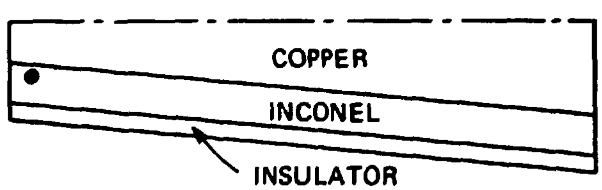

Table 9. Analysis conditions for various press models

Analysis input	Original analysis (press)	Revised analysis				
		100% Load			49% Load	
		Press	Half press	No press	Press	No press
Thickness, mm						
Copper	6.9/3.9	6.9/3.9	6.9/3.9	6.9/3.9	6.9/3.9	6.9/3.9
Inconel	3.5	3.5	3.5	3.5	3.5	3.5
Insulator	0.47	0.47	0.47	0.47	0.47	0.47
Width of inner leg, mm	230	230	230	230	230	230
Electromagnetic force						
Centering, GN/m^3	1.03	1.12	1.12	1.12	0.549	0.549
Hoop, kN/half turn	556	436	436	436	214	214
Preload, kN/half turn	−556	−436	−218	0	−214	0

Table 10. Comparison of stress (MPa) and strain (%) within copper at the inner surface for various press models

Stress and strain[a]	Original analysis (press)	Revised analysis				
		100% Load			49% Load	
		Press	Half press	No press	Press	No press
σ_f	−463	−505	−506	−511	−262	−258
σ_r	−138	−177	−188	−199	−21.9	−25.1
σ_v	−170	−215	−204	−199	−32.2	33.7
τ_{fr}	3.76	4.84	5.28	5.59	0.54	0.63
τ_{rv}	0	0	0	0	0	0
τ_{vf}	0	0	0	0	0	0
σ_{eq}	310	311	311	312	235	267
$\epsilon_{eq}^{(p)}$	0.31%	0.43%	0.53%	0.64%	0%	0.015%

[a]Subscripts f, r, and v indicate face compression direction, radial direction, and vertical direction, respectively.

ORNL–DWG 87-2314 FED

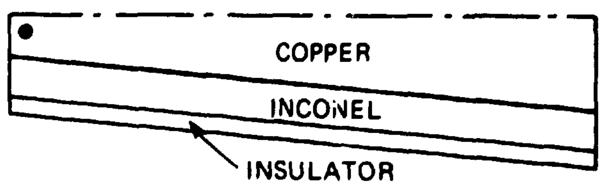

Table 11. Comparison of stress (MPa) and strain (%) within Inconel at the inner surface for various press models

Stress and strain[a]	Original analysis (press)	Revised analysis				
		100% Load			49% Load	
		Press	Half press	No press	Press	No press
σ_f	−478	−522	−529	−536	−264	−261
σ_r	210	265	288	305	39.9	44.3
σ_v	181	235	470	719	35.1	185
τ_{fr}	41.3	53.4	58.8	62.8	5.82	6.83
τ_{rv}	0	0	0	0	0	0
τ_{vf}	0	0	0	0	0	0
σ_{eq}	678	777	917	1113	302	395
$\epsilon_{eq}^{(p)}$	0%	0%	0%	0%	0%	0%

[a]Subscripts *f*, *r*, and *v* indicate face compression direction, radial direction, and vertical direction, respectively.

ORNL–DWG 87-2314A FED

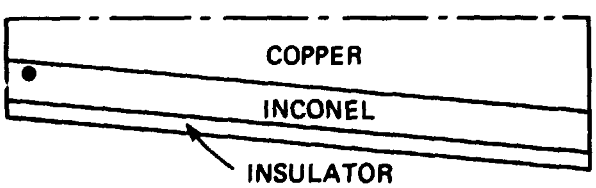

check the validity of the fraction of the composite. Table 12 summarizes the analysis conditions.

Tables 13 and 14 show the results in copper and Inconel, respectively. The equivalent plastic strain in the copper of the 1.6-m machine (57.5% copper) was about half that of the baseline machine, and the stress in the Inconel was about 15% less in the 1.6-m machine than in the baseline machine. The large machine (1.6 m) without preload, therefore, is better than the baseline (1.324 m) from the viewpoint of structural integrity. For the 1.6-m machine with 40% copper, the face compression stress was slightly increased, but the equivalent plastic strain in the copper was reduced 30% because the edge effect to extrude the copper at the end was smaller for the thinner copper composite. The copper fraction of 40%, therefore, is preferable to that of 57.7%.

Analyses were also made for 10 and 20% higher fields, with and without preload. Analysis conditions are summarized in Table 15. Preload value was fixed at 6×10^7 lb, which is the maximum capability of the press system. From Table 16, the equivalent strain in the copper is about twice that of the baseline design when a 10% higher field (10.64 T) is applied, and it is more than three times that of the baseline design for a 20% larger field (11.6 T). In the comparison between no-press and press cases, a preload of 6×10^7 lb compensates for the 10% increase in the field.

Table 12. Analysis conditions for the larger machines

Analysis input	Baseline, 57.5% Cu, press	R = 1.527 m, 57.5% Cu, no press	R = 1.6 m, 57.5% Cu, no press	R = 1.6 m, 40% Cu, no press
Thickness, mm				
Copper	6.9/3.9	8.0/3.6	8.0/4.0	6.19/2.19
Inconel	3.5	3.8	3.9	5.76
Insulator	0.47	0.51	0.53	0.53
Width of inner leg, mm	230	353	320	320
Electromagnetic force				
Centering, GN/m^3	1.12	0.632	0.695	1.00
Hoop, kN/half turn	436	431	481	481
Preload, kN/half turn	−436	0	0	0

Table 13. Comparison of stress (MPa) and strain (%) within copper at the inner surface for various larger machines

Stress and strain[a]	Baseline, 57.5% Cu, press	$R = 1.527$ m, 57.5% Cu, no press	$R = 1.6$ m, 57.5% Cu, no press	$R = 1.6$ m, 40% Cu, no press
σ_f	−505	−349	−386	−395
σ_r	−177	−71	−98	−114
σ_v	−215	−24	−61	−70
τ_{fr}	4.8	1.1	2.0	1.2
τ_{rv}	0	0	0	0
τ_{vf}	0	0	0	0
σ_{eq}	311	304	308	305
$\epsilon_{eq}^{(p)}$	0.43%	0.12%	0.22%	0.15%

[a]Subscripts f, r, and v indicate face compression direction, radial direction, and vertical direction, respectively.

ORNL–DWG 87-2314 FED

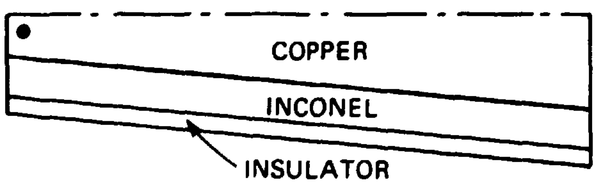

Table 14. Comparison of stress (MPa) and strain (%) within Inconel at the inner surface for various larger machines

Stress and strain[a]	Baseline, 57.5% Cu, press	$R = 1.527$ m, 57.5% Cu, no press	$R = 1.6$ m, 57.5% Cu, no press	$R = 1.6$ m, 40% Cu, no press
σ_f	−522	-354	−394	−400
σ_r	265	91	138	65.3
σ_v	235	272	372	255
τ_{fr}	53.4	12.0	21.7	12.1
τ_{rv}	0	0	0	0
τ_{vf}	0	0	0	0
σ_{eq}	777	558	681	584
$\epsilon_{eq}^{(p)}$	0%	0%	0%	0%

[a]Subscripts f, r, and v indicate face compression direction, radial direction, and vertical direction, respectively.

ORNL–DWG 87-2314A FED

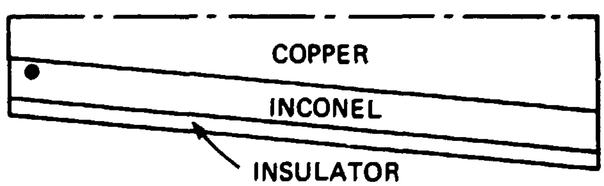

Table 15. Analysis conditions for the higher field cases with and without press system
(R = 1.6 m; 40% Cu)

Analysis input	No press			Press (6 × 10^7 lb)	
	9.67 T[a]	10.64 T	11.6 T	10.64 T	11.6 T
Thickness, mm					
Copper	6.19/2.19	6.19/2.19	6.19/2.19	6.19/2.19	6.19/2.19
Inconel	5.76	5.76	5.76	5.76	5.76
Insulator	0.53	0.53	0.53	0.53	0.53
Width of inner leg, mm	320	320	320	320	320
Electromagnetic force					
Centering, GN/m^3	1.00	1.21	1.44	1.21	1.44
Hoop, kN/half turn	481	582	693	582	693
Preload, kN/half turn	0	0	0	–529	–529

[a]Design field.

Table 16. Stress (MPa) and strain (%) for higher field cases with and without press system
(R = 1.6 m; 40% Cu)

Stress and strain	No press			Press (6 × 10^7 lb)	
	9.67 T[a]	10.64 T	11.6 T	10.64 T	11.6 T
			Copper		
σ_f	−395	−486	−586	−477	−574
σ_r	−114	−191	−283	−161	−252
σ_v	−70	−162	−267	−180	−277
τ_{fr}	1.2	2.1	3.1	1.7	2.8
τ_{rv}	0	0	0	0	0
τ_{vf}	0	0	0	0	0
σ_{eq}	305	310	311	307	310
$\epsilon_{eq}^{(p)}$	0.15%	0.31%	0.49%	0.19%	0.36%
			Inconel		
σ_f	−400	−492	−592	−481	−581
σ_r	65.3	106	155	89.3	138
σ_v	255	349	458	93.8	162
τ_{fr}	12.1	21.3	32.3	17.1	28.1
τ_{rv}	0	0	0	0	0
τ_{vf}	0	0	0	0	0
σ_{eq}	584	751	940	573	733
$\epsilon_{eq}^{(p)}$	0%	0%	0%	0%	0%

[a]Design field.

5. CONCLUSIONS

The effective Young's moduli of the composite are obtained accurately by elastic-plastic finite element analysis and the analytical equation and are useful for overall TF coil analysis by the three-dimensional elastic finite element method.

Stress and strain in the composite TF coils were examined by elastic-plastic finite element analyses for various CIT designs. Stress level is higher on the inner surface of the inner leg. Stress distribution through the composite has a peak on the interface. Plastic strain in the copper increases significantly with the out-of-plane force arising from a plasma disruption. The preload system is useful for the full loading operation of the baseline machine, whereas it is not needed for the 70% field operation. In the larger, alternative, pressless machines, stress and strain are lower than in the baseline machine. In the composite with the smaller copper fraction, the plastic strain in the copper is reduced because the edge effect is smaller. In the 1.6-m machine with a 40% copper fraction coil, a preload of 6×10^7 lb compensates for the 10% increase in magnetic field.

ACKNOWLEDGMENTS

The author greatly appreciates useful discussions with T. E. Shannon, T. G. Brown, V. D. Lee, and B. W. Riemer of the Fusion Engineering Design Center, Oak Ridge National Laboratory. Appreciation is also expressed to P. M. Stone of the U.S. Department of Energy and to K. Tomabechi, M. Yoshikawa, and S. Tamura of the Japan Atomic Energy Research Institute for arranging the author's assignment in the United States as part of the Japan–U.S. exchange program on the next-step fusion machine.

REFERENCES

1. *Compact Ignition Tokamak (CIT), Conceptual Design Report*, PPPL-A-860606-P-01, Princeton Plasma Physics Laboratory, Princeton, N.J., June 1986.

2. *MSC/NASTRAN Application Manual*, The MacNeal-Schwendler Corporation, Los Angeles, Calif., 1983.

3. J. Frankenberg and H. Murray, *Tensile and Hardness Data for the C107 Manufactured Revere*, PPPL EAD-1633, Princeton Plasma Physics Laboratory, Princeton, N.J., October 1986.

4. B. Riemer, *CIT TF Coil Stress Analyses*, Memorandum FEDC-M-87-SE-008, Martin Marietta Energy Systems, Inc., Oak Ridge Natl. Lab., February 1987.

5. S. Sackett, *EFFI—A Code for Calculating the Electromagnetic Field, Force, and Inductance in Coil Systems of Arbitrary Geometry*, UCID-17621, Lawrence Livermore National Laboratory, Livermore, Calif., May 1977.

6. H. Becker et al., *Structural Properties of Reinforced Copper*, PFC/RR-86-12, Massachusetts Institute of Technology, Cambridge, Mass., May 1986.

ORNL/FEDC-87/3
Dist. Category UC-20c,d

INTERNAL DISTRIBUTION

1. T. G. Brown
2. J. D. Galambos
3. M. L. Givens
4. J. R. Haines
5. P. N. Haubenreich
6–7. V. D. Lee
8. M. S. Lubell
9. B. W. Riemer
10. T. E. Shannon
11–12. Laboratory Records Department
13. Laboratory Records, ORNL-RC
14. Document Reference Section
15. Central Research Library
16. Fusion Energy Division Library
17–18. Fusion Energy Division Publications Office
19. ORNL Patent Office

EXTERNAL DISTRIBUTION

20. M. A. Abdou, Boelter Hall, University of California, Los Angeles, CA 90024
21. C. A. Anderson, Westinghouse Electric Corporation, Advanced Energy Systems Division, P.O. Box 158, Madison, PA 15663
22. J. L. Anderson, CMB-3, Mail Stop 348, Los Alamos National Laboratory, P.O. Box 1633, Los Alamos, NM 87545
23. C. C. Baker, Argonne National Laboratory, 9700 South Cass Avenue, Argonne, IL 60439
24. D. S. Beard, Office of Fusion Energy, Office of Energy Research, ER-531 Germantown, U.S. Department of Energy, Washington, DC 20545
25. K. L. Black, Department E452, McDonnell Douglas Astronautics Company, P.O. Box 516, St. Louis, MO 63166
26. R. Botwin, C47-05, Grumman Aerospace Corporation, P.O. Box 31, Bethpage, NY 11714
27. W. B. Briggs, McDonnell Douglas Astronautics Company, P.O. Box 516, St. Louis, MO 63166
28. J. N. Brooks, FPP/207, Argonne National Laboratory, 9700 South Cass Avenue, Argonne, IL 60439
29. S. C. Burnett, GA Technologies, Inc., P.O. Box 81608, San Diego, CA 92138
30. J. D. Callen, Department of Nuclear Engineering, University of Wisconsin, Madison, WI 53706
31. R. N. Cherdack, Burns and Roe, Inc., 800 Kinderkamack Road, Oradell, NJ 07649

32. J. F. Clarke, Director for Fusion Energy, Office of Energy Research, ER-50 Germantown, U.S. Department of Energy, Washington, DC 20545
33. D. R. Cohn, 167 Albany Street, NW 16-140, Massachusetts Institute of Technology, Cambridge, MA 02139
34. R. W. Conn, Department of Chemical, Nuclear, and Thermal Engineering, Boelter Hall, University of California, Los Angeles, CA 90024
35. J. G. Crocker, EG&G Idaho, P.O. Box 1625, Idaho Falls, ID 83401
36. G. R. Dalton, Department of Nuclear Engineering Science, Nuclear Science Center, University of Florida, Gainesville, FL 32611
37. R. C. Davidson, Massachusetts Institute of Technology, 77 Massachusetts Avenue, Cambridge, MA 02139
38. N. A. Davies, Office of the Associate Director, Office of Fusion Energy, Office of Energy Research, ER-51 Germantown, U.S. Department of Energy, Washington, DC 20545
39. S. O. Dean, Director, Fusion Power Associates, Inc., 2 Professional Drive, Suite 249, Gaithersburg, MD 20760
40. D. DeFreece, E451, Building 81/1/B7, McDonnell Douglas Astronautics Company, P.O. Box 516, St. Louis, MO 63166
41. J. N. Doggett, L-441, Lawrence Livermore National Laboratory, P.O. Box 5511, Livermore, CA 94550
42. H. Dreicer, Division Leader, CRT, Los Alamos National Laboratory, P.O. Box 1663, Los Alamos, NM 87545
43. F. Farfaletti-Casali, Engineering Division, Joint Research Center, Ispra Establishment, 21020 Ispra (Varese), Italy
44. P. A. Finn, Fusion Power Program, Argonne National Laboratory, 9700 South Cass Avenue, Argonne, IL 60439
45. H. K. Forsen, Bechtel Group, Inc., Research & Engineering, P.O. Box 3965, San Francisco, CA 94119
46. J. S. Foster, Jr., Building R4-2004, TRW Defense and Space Systems, 1 Space Park, Redondo Beach, CA 90278
47. T. K. Fowler, Associate Director for Magnetic Fusion Energy, L-436, Lawrence Livermore National Laboratory, P.O. Box 5511, Livermore, CA 94550
48. J. W. French, Princeton Plasma Physics Laboratory, P.O. Box 451, Princeton, NJ 08544
49. H. P. Furth, Director, Princeton Plasma Physics Laboratory, P.O. Box 451, Princeton, NJ 08544
50. J. G. Gavin, Jr., President, A01-11, Grumman Aerospace Corporation, P.O. Box 31, Bethpage, NY 11714
51. G. Gibson, Westinghouse Electric Corporation, Waltz Mill Site, P.O. Box 158, Madison, PA 15663

52. J. R. Gilleland, GA Technologies, Inc., Fusion and Advanced Technology, P.O. Box 81608, San Diego, CA 92138
53. M. Y. Gohar, Argonne National Laboratory, 9700 South Cass Avenue, Argonne, IL 60439
54. R. W. Gould, Department of Applied Physics, California Institute of Technology, Pasadena, CA 91125
55. R. A. Gross, Plasma Research Laboratory, Columbia University, New York, NY 10027
56. J. R. Haines, McDonnell Douglas Astronautics Company, St. Louis, MO 63166
57. C. D. Henning, Lawrence Livermore National Laboratory, P.O. Box 5511, Livermore, CA 94550
58. J. J. Holmes, Westinghouse-Hanford Engineering Development Laboratory, P.O. Box 1970, Richland, WA 99352

59–63. T. Horie, Japan Atomic Energy Research Institute, Tokai Research Establishment, Tokai-Mura, Naka-Gun, Ibaraki-ken 319-11, Japan

64. J. B. Joyce, Princeton Plasma Physics Laboratory, P.O. Box 451, Princeton, NJ 08544
65. R. A. Krakowski, CTR-12, Mail Stop 641, Los Alamos National Laboratory, P.O. Box 1663, Los Alamos, NM 87545
66. G. L. Kulcinski, University of Wisconsin, Department of Nuclear Engineering, Engineering Research Building, Room 439, 1500 Johnson Drive, Madison, WI 53706
67. D. L. Kummer, McDonnell Douglas Astronautics Company, P.O. Box 516, St. Louis, MO 63166
68. W. Marton, Office of Fusion Energy, Office of Energy Research, ER-55 Germantown, U.S. Department of Energy, Washington, DC 20545
69. L. G. Masson, EG&G Idaho, Idaho National Engineering Laboratory, P.O. Box 1625, Idaho Falls, ID 83401
70. D. M. Meade, Princeton Plasma Physics Laboratory, P.O. Box 451, Princeton, NJ 08544
71. A. T. Mense, Building 107, Post B2, McDonnell Douglas Astronautics Company, P.O. Box 516, St. Louis, MO 63166
72. R. W. Moir, Lawrence Livermore Laboratory, P.O. Box 5511, Livermore, CA 94550
73. D. B. Montgomery, MIT Plasma Fusion Center, 167 Albany Street, Cambridge, MA 02139
74. A. E. Munier, Grumman Aerospace Corporation, P.O. Box 31, Bethpage, NY 11714
75. R. E. Nygren, FPP/207, Argonne National Laboratory, 9700 South Cass Avenue, Argonne, IL 60439
76. T. Ohkawa, GA Technologies, Inc., P.O. Box 81608, San Diego, CA 92138

77. J. A. O'Toole, Princeton Plasma Physics Laboratory, James Forrestal Campus, Building I-P, Room 8A, P.O. Box 451, Princeton, NJ 08544
78. R. R. Parker, Francis Bitter National Magnet Laboratory, 170 Albany Street, Cambridge, MA 02139
79. B. Pease, Culham Laboratory, Abingdon, Oxfordshire OX14 3DB, United Kingdom
80. M. Pelovitz, Princeton Plasma Physics Laboratory, P.O. Box 451, Princeton, NJ 08544
81. F. W. Perkins, Princeton Plasma Physics Laboratory, P.O. Box 451, Princeton, NJ 08544
82. M. Porkolab, Massachusetts Institute of Technology, 77 Massachusetts Avenue, Cambridge, MA 02139
83. D. E. Post, Princeton Plasma Physics Laboratory, P.O. Box 451, Princeton, NJ 08544
84. R. E. Price, Office of Fusion Energy, Office of Energy Research, ER-55 Germantown, U.S. Department of Energy, Washington, DC 20545
85. F. A. Puhn, GA Technologies, Inc., P.O. Box 81608, San Diego, CA 92138
86. R. V. Pyle, University of California, Lawrence Berkeley Laboratory, Berkeley, CA 94720
87. J. M. Rawls, GA Technologies, Inc., P.O. Box 81608, San Diego, CA 92138
88. M. Roberts, International Program, Office of Fusion Energy, Office of Energy Research, ER-52 Germantown, U.S. Department of Energy, Washington, DC 20545
89. J. D. Rogers, Los Alamos National Laboratory, P.O. Box 1663, Los Alamos, NM 87545
90. M. L. Rogers, Monsanto Research Corporation, Mound Laboratory Facility, P.O. Box 32, Miamisburg, OH 45342
91. M. N. Rosenbluth, RLM 11.218, Institute for Fusion Studies, University of Texas, Austin, TX 78712
92. P. H. Rutherford, Princeton Plasma Physics Laboratory, P.O. Box 451, Princeton, NJ 08544
93. J. A. Schmidt, Princeton Plasma Physics Laboratory, P.O. Box 451, Princeton, NJ 08544
94. J. Schultz, MIT Plasma Fusion Center, 167 Albany Street, Cambridge, MA 02139
95. F. R. Scott, Electric Power Research Institute, P.O. Box 10412, Palo Alto, CA 94304
96. G. Sheffield, Princeton Plasma Physics Laboratory, P.O. Box 451, Princeton, NJ 08544
97. D. Smith, Materials Science Division, Argonne National Laboratory, 9700 South Cass Avenue, Argonne, IL 60439

98. W. M. Stacey, Jr., Georgia Institute of Technology, School of Nuclear Engineering and Health Physics, Atlanta, GA 30332
99. D. Steiner, Rensselaer Polytechnic Institute, Nuclear Engineering Department, NES Building, Tibbets Avenue, Troy, NY 12181
100. E. Stern, Grumman Aerospace Corporation, CN-59, Forrestal Campus, Princeton, NJ 08544
101. P. M. Stone, Fusion Systems Design Branch, Division of Development and Technology, Office of Fusion Energy, Office of Energy Research, ER-532 Germantown, U.S. Department of Energy, Washington, DC 20545
102. I. N. Sviatoslavsky, Room 33, Engineering Research Building, 1500 Johnson Drive, University of Wisconsin, Madison, WI 53706
103. R. E. Tatro, Manager, Energy Systems, M.Z. 16-1070, General Dynamics-Convair Division, P.O. Box 80847, San Diego, CA 92138
104. F. Thomas, B-20-5, Grumman Aerospace Corporation, Bethpage, NY 11714
105. K. I. Thomassen, Lawrence Livermore National Laboratory, P.O. Box 5511, Livermore, CA 94550
106. R. J. Thome, Francis Bitter National Magnet Laboratory, 170 Albany Street, Cambridge, MA 02139
107. C. Trachsel, McDonnell Douglas Astronautics Company, P.O. Box 516, St. Louis, MO 63166
108. A. W. Trivelpiece, Office of Energy Research, U.S. Department of Energy, Washington, DC 20545
109. L. R. Turner, Fusion Power Program, Argonne National Laboratory, 9700 South Cass Avenue, Argonne, IL 60439
110. E. H. Valeo, Princeton Plasma Physics Laboratory, P.O. Box 451, Princeton, NJ 08544
111. R. Varma, Physical Research Laboratory, Navrangpura, Ahmedabad 380009, India
112. J. C. Wesley, GA Technologies, Inc., P.O. Box 81608, San Diego, CA 92138
113. J. E. C. Williams, Francis Bitter National Magnet Laboratory, 170 Albany Street, Cambridge, MA 02139
114. H. H. Yoshikawa, W/A-62, Hanford Engineering Development Laboratory, P.O. Box 1970, Richland, WA 99352
115. K. M. Young, Princeton Plasma Physics Laboratory, P.O. Box 451, Princeton, NJ 08544
116. N. E. Young, Princeton Plasma Physics Laboratory, P.O. Box 451, Princeton, NJ 08544
117. Bibliothek, Max-Planck Institut fur Plasmaphysik, D-8046 Garching, Federal Republic of Germany
118. Bibliothek, Institut fur Plasmaphysik, KFA, Postfach 1913, D-5170 Julich, Federal Republic of Germany

119. F. Prevot, CEN/Cadarache, Departement de Recherches sur la Fusion Controlee, 13108 Saint-Paul-lez-Durance, France
120. Documentation S.I.G.N., Departement de la Physique du Plasma et de la Fusion Controlee, Association EURATOM-CEA, Centre d'Etudes Nucleaires, B.P. 85, Centre du Tri, 38041 Grenoble Cedex, France
121. Library, Centre de Recherches en Physique des Plasmas, 21 Avenue des Bains, 1007 Lausanne, Switzerland
122. Library, Culham Laboratory, UKAEA, Abingdon, Oxfordshire, OX14 3DB, England
123. Library, FOM Instituut voor Plasmafysica, Rijnhuizen, Edisonbaan 14, NL-3430 Nieuwegein, The Netherlands
124. J. Shang-Xian, Graduate School, Academia Sinica, P.O. Box 3908, Beijing, China (PRC)
125. Library, Institute for Plasma Physics, Nagoya University, Nagoya 464, Japan
126. Library, International Centre for Theoretical Physics, Trieste, Italy
127. Library, JET Joint Undertaking, Abingdon, Oxfordshire, OX14 3EA, England
128. Library, Laboratorio Gas Ionizzati, CP 65, 00044 Frascati, Rome, Italy
129. Plasma Research Laboratory, Australian National Laboratory, P.O. Box 4, Canberra, ACT 2000, Australia
130. Thermonuclear Library, Japan Atomic Energy Research Institute, Tokai Research Establishment, Tokai-Mura, Naka-Gun, Ibaraki-ken 319-11, Japan
131. Library, Plasma Physics Laboratory, Kyoto University, Gokasho, Uji, Kyoto 611, Japan
132. Office of the Assistant Manager for Energy Research and Development, U.S. Department of Energy, Oak Ridge Operations, P.O. Box E, Oak Ridge, TN 37831

133–274. Given distribution as shown in TIC-4500, Magnetic Fusion Energy (Distribution Category UC-20 c,d: Reactor Materials and Fusion Systems)